Determination of the nearest-neighbor interaction in VO_2 via fractal dimension analysis

Jacob Holder,* Daniel Kazenwadel,* Peter Nielaba, and Peter Baum†
Universität Konstanz, Fachbereich Physik, 78464 Konstanz, Germany

(Received 2 February 2023; revised 19 October 2023; accepted 14 November 2023; published 20 December 2023)

The Ising model is one of the simplest and most well-established concepts to simulate phase transformations in complex materials. However, its most central constant, the interaction strength $\boldsymbol{J}$ between two nearest neighbors, is hard to obtain. Here we show how this basic constant can be determined with a fractal dimension analysis of measured domain structures. We apply this approach to vanadium dioxide, a strongly correlated material with a first-order insulator-to-metal phase transition with enigmatic properties. We obtain a nearest-neighbor interaction of 13.8 meV, a value close to the thermal energy at room temperature. Consequently, even far below the transition temperature, there are spontaneous local phase flips from the insulating into the metallic phase. These fluctuations explain several measured anomalies in VO_2, in particular the low thermal carrier activation energy and the finite conductivity of the insulating phase. As a method, our fractal dimension analysis links the Ising model to macroscopic material constants for almost any first-order phase transition.

DOI: 10.1103/PhysRevResearch.5.043272

I. INTRODUCTION

Phase transitions are a fascinating branch of physics because a wealth of distinctive phenomena can emerge in macroscopic objects from rather simple sets of atomistic interactions. While thermodynamics drives a material into disorder and randomness, the cooperativity between neighboring elements, for example the spins in magnetic materials or adjacent unit cells in crystals, favors self-organization and leads to spontaneous symmetry breaks into intricate domain structures. The Ising model [1] is one of the simplest and most well-established theories [2,3] to understand phase transitions from an atomistic perspective. Basically, multiple discrete elements or cells in an array interact cooperatively with their nearest neighbors while temperature provides a perturbing force. Besides its original use in magnetism [4–6], the Ising model is applied for crystallization and nucleation [7–10], genetics [11], and even social sciences [12]. However, its central constant, the nearest-neighbor interaction J, is in most cases not well related to any measurable property of a macroscopic material, and therefore hard to obtain. This lack substantially limits the applicability of the Ising model to predict or understand the properties of a material.

In this work, we report how to use a fractal dimension analysis of a measured macroscopic domain pattern to determine the underlying nearest-neighbor interaction J in a quantitative way on atomistic dimensions. To elucidate the idea of the approach, Fig. 1 depicts a material with two phases (black and white) at a temperature close to a first-order phase transition. At otherwise identical conditions, the interaction strength J is increased from left to right, causing the macroscopic domain structure to favor more and more consolidated configurations with reduced surface roughness. This consolidation shows itself as a decrease of the fractal dimension, that is, the scaling behavior of the perimeter-to-area ratio of the domains. The idea of this work is to link, by comparison of an atomistic Ising model with measured domain shapes, the microscopic coupling J to a set of measurable quantities from a macroscopic experiment.

We demonstrate our approach on the example of vanadium dioxide (VO_2), a strongly correlated material with a notable first-order phase transition from monoclinic/insulator to rutile/metallic at a temperature of $T_t \approx 340\,\mathrm{K}$ [13], slightly above room temperature. This phase transition is not only relevant for technological applications, for example thermochromic windows [14–16], ultrafast photoelectric switches [17,18], ultrasensitive bolometers [19], or impulse strain-wave emitters [20], but it is also of great interest to fundamental physics, because the atomistic transition proceeds on nontrivial reaction paths [21–24] and the strongly correlated nature of the material [25] can bring even advanced *ab initio* calculations [26–28] close to the edges of their applicability range. Although VO_2 has been heavily investigated [13–40], there remain many open questions, in particular why insulating VO_2 has several orders of magnitude higher electrical conductivity than estimated from the band gap [29–34], and why there is an unexpected upper limit for it [35,36]. Experiments with Kelvin probe force microscopy (KPFM) [37] and scanning near-field infrared microscopy (SNOM) [38] have revealed a complex set of domain patterns that will be the experimental basis of our report. Similar patterns are observed after laser excitation on ultrafast time scales [39,40].

*These authors contributed equally to this work.
†peter.baum@uni-konstanz.de

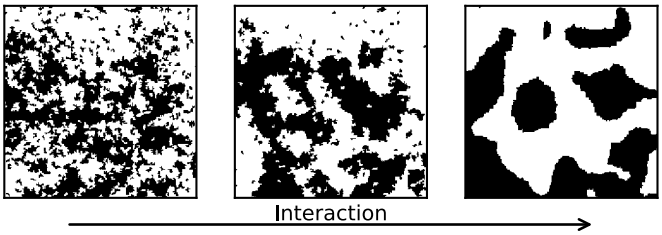

FIG. 1. Influence of interaction J on domain formation. Left to right, typical domain patterns in a two-phase material for increasing nearest-neighbor interaction J. For small J (left), neighboring cells hardly interact with each other, favoring a nearly random domain structure and jagged surfaces. For intermediate J (middle), intricate domains form via the interplay of random flips from temperature and the cooperativity between adjacent cells. For high J (right), the cooperative interactions dominate and produce well-defined domains with smooth surfaces. The ratio between the black and white phases is ∼50% in all pictures, but they differ in their fractal geometry.

II. FRACTAL DIMENSION ANALYSIS

Let us first consider the general approach of our fractal dimension analysis and discuss the physical implications at a later stage. We consider a material with two phases and describe its microscopic behavior with an Ising model in which neighboring unit cells show some effective cooperativity. We use a cubic lattice and identify the two phases (for example metal and insulator) with the two states $\sigma_i = \pm 1$ of the Ising system. Each unit cell of the crystal is associated with one cell in the Ising model. The nearest-neighbor interaction J denotes the energy it takes when two neighboring cells are in different phases. The temperature T in the material is considered via the free energy of a unit cell, approximated as $h(T) = L\frac{T_t - T}{T_t}$, where T_t is the transition temperature. This can be derived using the Helmholtz free energy $F = U - TS$ [41] of a first-order phase transition with the latent heat $L = T\Delta S$. The resulting energy bias is zero for cells in any phase at the transition temperature T_t but linearly favors the "correct" phase for cells with a temperature difference $T_t - T$. The resulting Hamiltonian H of our Ising model is

$$H = -\frac{1}{2}\sum_{i,j\in \mathrm{NN}} J\,\sigma_i\sigma_j + \sum_i h_i(T)\sigma_i, \qquad (1)$$

where σ_i is the state at position i and σ_j are all the nearest neighbors at positions j. The factor of $\frac{1}{2}$ accounts for the double summation. Note that the energy to create a domain wall in the Ising model is $2J$ because $\sigma_i\sigma_j$ jumps from -1 to $+1$. All parameters except J are available from experiments; the values for VO_2 are given in Table I.

TABLE I. Parameters in our simulations of VO_2.

System parameter	Value	Reference
Transition temperature T_t	340 K	[13]
Standard deviation ΔT_t	0.25 K	[38,42]
Latent heat L	51 J/g ≈ 3 $k_B T_t$	[43]
Unit cell size	0.5 nm	[44]
Grain size	90 nm	[42]

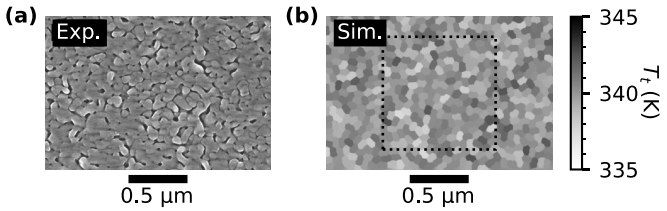

FIG. 2. Generation of the grain-induced bias of the transition temperature. (a) Scanning electron microscopy image of a VO_2 thin film prepared by sol-gel deposition, reproduced from Ref. [42]. Even after substantial annealing efforts, slightly different grains are still distinguishable. Black to white, secondary electron emission current. (b) Model for the distribution of transition temperature T_t in our simulations (see Appendix). The dotted lines indicate the area used for the analysis in Fig. 3.

Realistic materials in condensed-matter physics are often not perfect crystals but have inhomogeneities on nanometer and micrometer dimensions, for example, small variations of density, strain, or stoichiometry. Such inhomogeneities often slightly change the local transition temperature, and T_t therefore becomes a function of position within the material. Without such deviations, the hysteresis would be infinitely sharp and no domains would be observed. In our Ising model, we consider a finite steepness of the hysteresis curve by assigning a normal-distributed T_t with a width ΔT_t to each cell in a way that mimics the typical nanostructure of a realistic material. Figure 2(a) shows a measured scanning-electron-microscopy image of a polycrystalline thin film of VO_2 and Fig. 2(b) depicts the granular T_t map that we use in our simulations (Appendix). While the existence of a finite bias width is central to our approach, its specific value or the particular distribution into grains does not affect the fractal domain geometry and its link to J (Appendix).

We use the Metropolis Monte Carlo algorithm [45] to generate equilibrated sample states for different interactions and temperatures. We simulate a three-dimensional volume of $2000 \times 2000 \times 120$ unit cells ($1000 \times 1000 \times 60\,\mathrm{nm}^3$) with six nearest neighbors per cell and alternatively a two-dimensional area with 2000×2000 unit cells ($1000 \times 1000\,\mathrm{nm}^2$) with four nearest neighbors per cell. For each configuration and initialization, we conduct 5000 Monte Carlo sweeps, found to be sufficient for reaching equilibrium. One typical three-dimensional (3D) simulation takes ∼640 core hours on the supercomputer JUWELS in Jülich while a typical 2D simulation takes only ∼40 core hours on a desktop computer.

Figure 3 shows in the middle two columns a set of simulated domain configurations. In comparison, the left and right columns show measurement results from Kelvin probe force microscopy (KPFM) and scanning near-field optical microscopy (SNOM), reprinted from Refs. [37,38]. From top to bottom, the temperature is increased. We see that our Ising simulations and the two experimental data sets produce comparable results. The slight discrepancies in the SNOM measurements (right column) are explained by the finite probing depths of ∼50 nm in SNOM [46] as compared to <1 nm in KPFM [47].

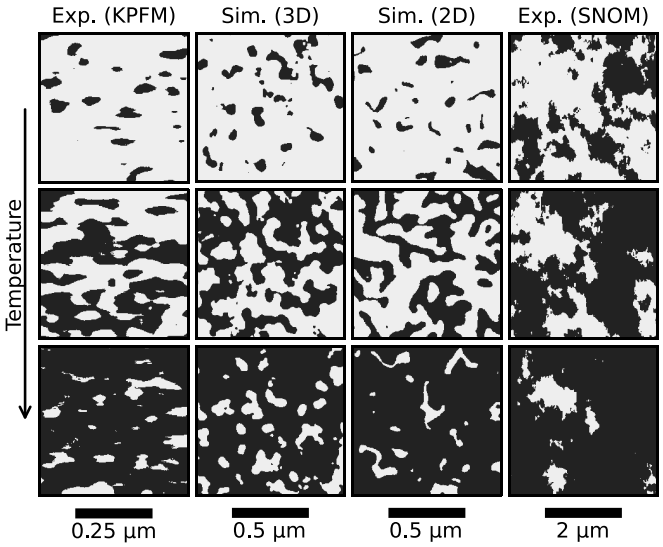

FIG. 3. Measured and simulated domain structure of VO_2 thin films at different temperatures. Black, metallic phase; white, insulator phase. Top to bottom, increasing temperature, calibrated by the ratio of phase coverage. KPFM, Kelvin probe force microscopy (left column); SNOM, scanning near-field optical microscopy (right column); data reproduced from Refs. [37,38]. In the 3D simulations, we plot only the topmost layer. Besides slight measurement artifacts, such as line scanning effects in KPFM and nonvanishing depth information in SNOM, the measured and simulated fractal geometries are in good agreement.

Sohn *et al.* [37] have found in their experiments on thin films that the domain patterns have a fractal shape and therefore the ratio of perimeter to area follows a power law. To find the microscopic interaction strength J on atomistic dimensions, a metric is needed to compare the simulated domain patterns from the Ising model with the experimental results. Figure 4(a) depicts our approach: we numerically determine the domain perimeter and domain area for each measured or simulated domain with depth-first search; data are not sorted by temperature in this approach. Figure 4(b) shows the results for the two experiments (dots and squares). We see that all data points lie on a linear curve in a log-log plot, indicating a power law that is consistent over four orders of magnitude, independently of temperature. The slight constant offset between the two data sets is irrelevant because it relates only to a smoothing of the perimeter by experimental resolution effects.

In order to determine the fractional exponent, we fit the perimeter-to-area distribution of Fig. 4 by linear regression, weighted by inverse density via Kernel density estimation [48,49] to account for the inhomogeneous size distribution of the domain clusters; there are typically many small ones and few large ones. Finite-size effects [50,51] from the experimental resolution or the discrete nature of the Ising model are avoided by disregarding domains with areas below $10^3\,\mathrm{nm}^2$ for KPFM, below $10^5\,\mathrm{nm}^2$ for SNOM, and below $50\,\mathrm{nm}^2$ in the simulations. We define the fractal dimension D as the slope of the linear fits in the log-log plot. It is related to the Hausdorff dimension D_H [52] used in Ref. [37] by a factor of two, that is, $D_\mathrm{H} = 2D$; compare Refs. [53–55]. We obtain $D_\mathrm{KPFM} = 0.72$ and $D_\mathrm{SNOM} = 0.71$. These almost identical results, obtained with completely unrelated experimental methods, KPFM and SNOM, on rather different thin-film materials, produced with pulsed laser deposition [37] or the sol-gel method [38], show that the fractal dimension of a two-phase material is indeed a robust material constant in the investigated ranges.

The fractal dimension of a domain pattern, accessible to experiments, is therefore a robust and solid basis for our next step, the extraction of a value for the microscopic interaction. Figure 4(c) shows a fractal dimension analysis of simulated domain configurations from our Ising model as a function of an increasing interaction J. Using the identical analysis procedure as described above, we find the same power laws as in the experiments. We see that the fractal dimension D of the simulated data sets strongly depends on the atomistic interaction parameter J. With decreasing J (blue), the domain perimeters become more and more irregular and jagged, resulting in a higher D, while a larger J (green) produces more roundish domains, resulting in a smaller D (compare Fig. 1).

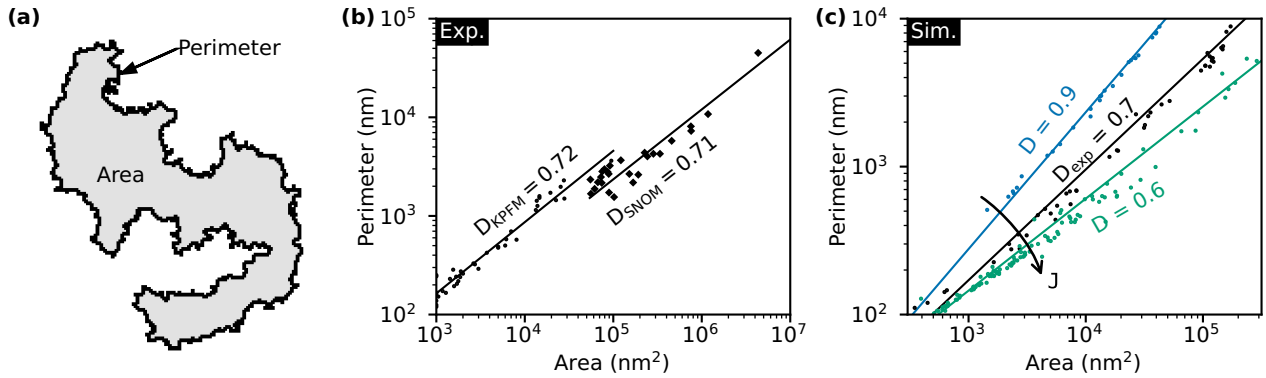

FIG. 4. Area dependence of the perimeter distribution and analysis of fractal dimensions. (a) Definition of area and perimeter. (b) Experimental data from Kelvin probe force microscopy (dots) and scanning near-field optical microscopy (squares). Self-similarity results in a power law behavior (linear in the log-log plot) in both cases (solid lines). The averaged fractal dimension (the slope) in the two experiments is $D_\mathrm{exp} = 0.715$. (c) Same data from our three-dimensional Ising model for increasing interaction J (blue, black, green) together with the resulting fractal dimensions D. The black result corresponds best to the experiment.

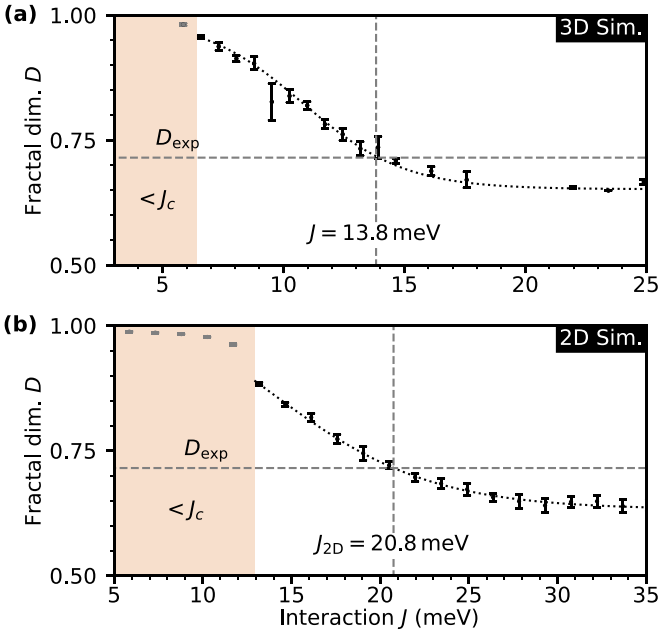

FIG. 5. Determination of nearest-neighbor interactions J from fractal dimensions D. (a) Results of a set of three-dimensional simulations; we obtain $J \approx 13.8$ meV for the measured D_{exp} (dashed lines). Error bars, standard deviation of five independent simulations. The dotted line is a logistic fit to the data; we exclude data points below the critical interaction J_C where the cells become uncorrelated (orange). (b) Results of a set of two-dimensional simulations; we obtain an effective $J_{2D} \approx 20.8$ meV (dashed lines).

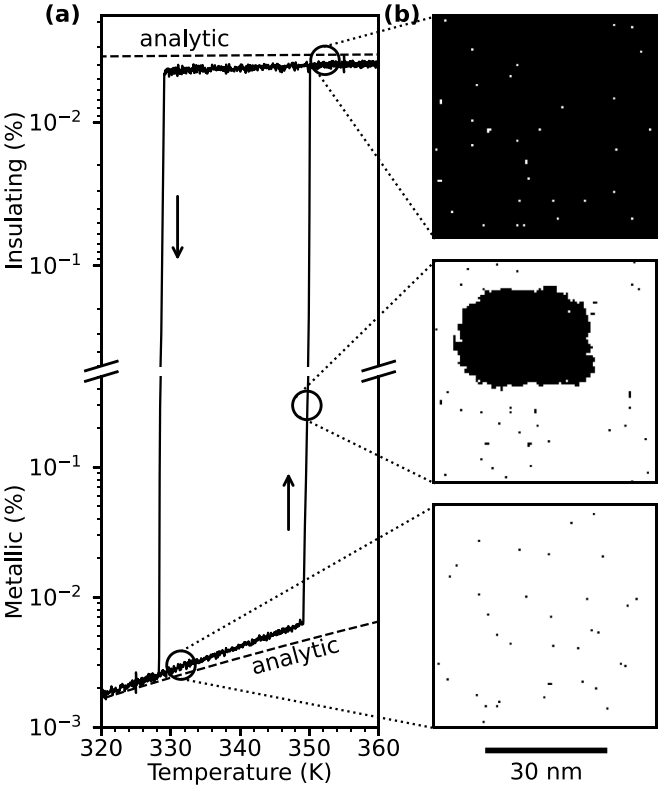

FIG. 6. Average fraction of metallic respectively insulating phase as a function of temperature. (a) Fraction of the individual minority phase across the hysteresis curve. When approaching the transition from low temperatures (upwards arrow), there is an increasing amount of metallic unit cells in an otherwise insulating material. The dashed line shows our analytic result from the Hamiltonian of Eq. (1). The slight deviations when approaching the phase jump are due to double-cell or multicell fluctuation events. A similar behavior occurs during cooling (downward arrow). (b) Real-space snapshots of the simulated phase maps for three selected temperatures [57]. Bottom, below the transition temperature; middle, after nucleation of a first stable bigger domain; top, far above the transition. Here, the fluctuations are similar but reversed as compared to the low-temperature phase. White denotes insulating/monoclinic unit cells, black denotes metallic/rutile unit cells.

Figure 5(a) shows the dependency between D and J as obtained from the simulations. Each data point is the average of five independent simulations; the error bar denotes the standard deviation. For a very high interaction, the domains become nearly circular and the fractal dimension eventually approaches $1/2$. For zero interaction, each cell is completely independent of its neighbors and the fractal dimension approaches 1. Between these limits, we find that the dependency of D on J can be approximated with the logistic function (dotted line). Reproducing the measured fractal geometry $D_{exp} = 0.715$ requires a nearest-neighbor interaction of $J = 13.8$ meV.

In order to describe thin-films or monolayers at much shorter computation times, we alternatively invoke a two-dimensional simulation; the analysis procedure remains the same. Figure 5(b) shows the results. Again, we see a characteristic increase of the fractal dimensions D with J that allows us to extract a value for the effective two-dimensional interaction; we obtain $J_{2D} = 20.8$ meV. Interestingly, this value relates to the 3D result by a factor of roughly 6/4, the ratio of the numbers of nearest neighbors.

III. IMPLICATIONS FOR VO_2

We now discuss the immediate physical consequences of our results on VO_2. Close to room temperature, when the material is in principle in the insulating phase, our simulations reveal a substantial percentage of single unit cells that are, for tiny amounts of time, fluctuating into the metallic phase. However, each of these spontaneously flipped unit cells is unstable and rapidly flips back. We can now use the measured $J = 13.8$ meV to predict quantitatively the fraction of such cells. The activation energy for the creation of a single rutile/metallic unit cell in an otherwise monoclinic/insulating material is $E_{act} \approx 6 \times 2J = 166$ meV. Below the transition, we obtain the average fraction $P_{metal} = e^{-E_{act}/k_B T}$ of metallic unit cells. For example, at room temperature at $T = 300$ K, about 40 K below T_t, where the entire crystal appears completely insulating in the measurements [29], these fluctuations amount to 1‰, averaged over space and time. This level of fluctuations corresponds nicely to the measured carrier density at room temperature from Hall experiments [34,56].

Figure 6 shows the phase distributions between metallic/rutile and insulating/monoclinic at different sample temperatures in the simulations. Figure 6(a) shows the average fraction of the minority phase as a function of temperature

and Fig. 6(b) shows snapshots of the simulated sample area at selected times. As the temperature increases, more and more unit cells flip, thermally activated, into the metallic phase and back [bottom of Fig. 6(b)]. The dashed line shows the expected amount of metallic unit cells as calculated analytically for flips of single unit cells. Far below the transition, it reproduces the simulated behavior. Closer to the transition there appear deviations due to the contributions of fluctuating double-cell and multicell nanodomains.

At a certain threshold (here 350 K), the first stable metallic domain emerges [middle of Fig. 6(b)] and rapidly grows, triggering a fast transformation of the complete material (upwards arrow). In the high-temperature phase, the metallic/rutile material [top of Fig. 6(b)] fluctuates back into the insulating/monoclinic phase (white dots) at a similar rate as in the opposite, insulating case. The slope of the fluctuations is now lower, because a rising temperature results in higher available thermal energies but also higher flipping barriers [see second part of Eq. (1)]. When the sample is cooled down, it transforms back into the insulating phase (downward arrow) with an insulating/monoclinic phase nucleus (white). The width of the simulated hysteresis depends on the speed of the cooling and heating processes. A movie of these fluctuations and the corresponding phase percentages during heating and cooling is provided in the Supplemental Material [57].

The existence of these surprisingly substantial thermal phase fluctuations far below the transition temperatures offers an elegant explanation of diverse reported anomalies of VO_2. For example, insulating VO_2 has an optically measured band gap of 600 meV [58,59] and the material should therefore be a good insulator with an electrical activation energy of ∼300 meV [34,35]. However, many experiments [29–34] report substantially lower values of 90–190 meV, for example, in nanorods (90 meV [29]), nanowires (128 meV [30]), thin films on sapphire (76 meV [31], 168 meV [32]), thin films on Ge (180 meV [31], 190 meV [33]), thin-films on Si (190 meV [33]), and bulk (100–650 meV [34]). Only experiments on extremely thin films [60] and nanobeams [35] report values of 225–310 and 300 meV, respectively.

In our simple and approximate model, the structural activation energy of rutile/metallic unit cells is $E_{act} \approx 6 \times 2J = 166$ meV. If we assume that a material with fluctuating unit cells has a carrier concentration that is the average of the individual unit cells (mean material), many of the experimental results can be reproduced, although some of the experiments are made on samples without fractal domains. We argue that the steady-state carrier densities in insulating/monoclinic VO_2 are the direct result of spontaneous and quick structural unit cell fluctuations into the metallic/rutile phase and back. If so, band gap effects, special energy levels, doping, defects, or edge effects are not required to explain the high conductivity of insulating VO_2. The observed decrease of conductivity in strained materials [34,35] fits into the picture, because closer proximity between adjacent unit cells increases the structural coupling J and therefore increases the activation energy for metallic unit cells, reducing their number. In VO_2 nanorods with domain coexistence, there is a surprising upper limit for the conductivity of the insulating parts [35,36]. Our model of phase fluctuations can explain this result via classical nucleation theory, because only a maximum amount of metallic unit cells can exist within an insulating domain until they nucleate and transform into a macroscopic metallic domain.

In the high-temperature phase, experiments have revealed an increase in electrical conductivity with increasing temperature [33,61,62], opposite to the behavior of normal metals. Our model naturally predicts this effect: Slightly above the transition temperature, there are lots of fluctuating insulating/monoclinic unit cells that act as defects and reduce the electrical conductivity. At higher temperatures above the transition temperature, these fluctuations are more and more suppressed [see Fig. 6(a)]. Consequently, electrical conductivity increases with rising temperature.

The reported spontaneous phase fluctuations affect not only the electronic but also the mechanical properties of VO_2: When approaching the phase transition, VO_2 becomes soft in terms of an increasing lattice elasticity [63], because the higher amount of structural phase fluctuations at higher temperatures allows the material to react more softly to mechanical strain. A generalized Ising model (Potts model) can be applied if other low-temperature phases, external strain [64], stripe formation [65], twinning or related effects shall be simulated as well. To confirm or invalidate the generality of our Ising model and fluctuation results for VO_2 samples in other than thin-film geometries, more experiments will be appropriate.

IV. CONCLUSIONS

In summary, our fractal dimension analysis of macroscopic experimental domain structures from thin-film specimen provides a robust and reproducible material constant, the fractal dimension, that we can relate to the most central parameter of the Ising model, the microscopic cooperativity between adjacent unit cells. This direct access to the interaction strength enables coarse-grained simulations of almost any material with fractal domain structures in a quantitative way. All material parameters that are needed for the reported procedure are quite basic and obtainable for a manifold of other phase-change materials as well. Morphologies or defects that only impact the local transition temperature are insignificant to our results, and fractional dimension analysis therefore gives extrapolated access to the properties of the ideal material. Quantitative knowledge of atomistic nearest-neighbor interactions links the Ising model to macroscopic quantities of a material, such as the absolute energy cost for the formation of domain boundaries, and also provides insight into fluctuation effects. These abilities will help to elucidate the emergence of macroscopic phase diagrams from microscopic phenomena and link the dynamics of phase transitions to atomistic processes in space and time.

ACKNOWLEDGMENTS

We thank A. Sohn and D.-W. Kim for sharing the data reproduced in Fig. 4, and A. Lüders for providing dumbbell shapes. We acknowledge financial support by the Evangelisches Studienwerk e.V. and the Deutsche Forschungsgemeinschaft through Sonderforschungsbereich SFB 1432. We gratefully acknowledge the computing time granted by

the John von Neumann Institute for Computing (NIC) on JUWELS at the Jülich Supercomputing Centre (JSC).

APPENDIX: MODELING OF CRYSTAL NANOSTRUCTURES

For simulating inhomogeneous crystals with varying T_t [see Fig. 2(a)] we use a 90% volume fraction of dumbbell colloids with an aspect ratio of 1.55 [66] to represent the different grains. The dumbbells have a length of 90 nm [42]. Each grain gets a transition temperature normally distributed around T_t with a width of $\Delta T_t = 0.25$ K, estimated from measured hysteresis curves [38,42]. We close the remaining holes in the T_t map by cubic interpolation and ensure periodic boundaries by stitching of mirror images. Figure 1(b) shows the results. Variations of ΔT_t or different grain sizes do not affect our simulations, even when the grain size becomes as small as one unit cell. Although perfect bulk single crystals cannot be used for our procedure because the domains are as large as the entire material, the robustness of our results over three to four orders of magnitude of domain sizes [see Fig. 4(b)] indicates the applicability of our evaluated J for single crystals on millimeter dimensions [67]. Materials in which anisotropic external strain is dominant [64,65] could be incorporated into our model by a generalized Ising Hamiltonian.

[1] E. Ising, Beitrag zur Theorie des Ferromagnetismus, Z. Phys. **31**, 253 (1925).

[2] L. Onsager, Crystal statistics. I. A two-dimensional model with an order-disorder transition, Phys. Rev. **65**, 117 (1944).

[3] R. Peierls, On Ising's model of ferromagnetism, Math. Proc. Cambridge Philos. Soc. **32**, 477 (1936).

[4] H. A. Kramers and G. H. Wannier, Statistics of the two-dimensional ferromagnet. part I, Phys. Rev. **60**, 252 (1941).

[5] J.-U. Lee, S. Lee, J. H. Ryoo, S. Kang, T. Y. Kim, P. Kim, C.-H. Park, J.-G. Park, and H. Cheong, Ising-type magnetic ordering in atomically thin $FePs_3$, Nano Lett. **16**, 7433 (2016).

[6] R. Soto, G. Martinez, M. N. Baibich, J. M. Florez, and P. Vargas, Metastable states in the triangular-lattice Ising model studied by Monte Carlo simulations: Application to the spin-chain compound $Ca_3Co_2O_6$, Phys. Rev. B **79**, 184422 (2009).

[7] D. Schebarchov, T. P. Schulze, and S. C. Hendy, Degenerate Ising model for atomistic simulation of crystal-melt interfaces, J. Chem. Phys. **140**, 074704 (2014).

[8] D. Eaton, I. Saika-Voivod, R. K. Bowles, and P. H. Poole, Free energy surface of two-step nucleation, J. Chem. Phys. **154**, 234507 (2021).

[9] R. Schmid and P. Nielaba, Stability of nanoparticles in solution: A statistical description of crystallization as a finite particle size effect in a lattice-gas model, J. Chem. Phys. **150**, 054504 (2019).

[10] J. Holder, R. Schmid, and P. Nielaba, Two-step nucleation in confined geometry: Phase diagram of finite particles on a lattice gas model, J. Chem. Phys. **156**, 124504 (2022).

[11] J. Majewski, H. Li, and J. Ott, The Ising model in physics and statistical genetics, Am. Hum. Genet. **69**, 853 (2001).

[12] A. Lipowski, D. Lipowska, and A. L. Ferreira, Phase transition and power-law coarsening in an Ising-doped voter model, Phys. Rev. E **96**, 032145 (2017).

[13] F. J. Morin, Oxides which show a metal-to-insulator transition at the Neel temperature, Phys. Rev. Lett. **3**, 34 (1959).

[14] Y. Cui, Y. Ke, C. Liu, Z. Chen, N. Wang, L. Zhang, Y. Zhou, S. Wang, Y. Gao, and Y. Long, Thermochromic VO_2 for energy-efficient smart windows, Joule **2**, 1707 (2018).

[15] S. Wang, T. Jiang, Y. Meng, R. Yang, G. Tan, and Y. Long, Scalable thermochromic smart windows with passive radiative cooling regulation, Science **374**, 1501 (2021).

[16] K. Tang, K. Dong, J. Li, M. P. Gordon, F. G. Reichertz, H. Kim, Y. Rho, Q. Wang, C.-Y. Lin, C. P. Grigoropoulos, A. Javey, J. J. Urban, J. Yao, R. Levinson, and J. Wu, Temperature-adaptive radiative coating for all-season household thermal regulation, Science **374**, 1504 (2021).

[17] C. Lu, Q. Lu, M. Gao, and Y. Lin, Dynamic manipulation of THz waves enabled by phase-transition VO_2 thin film, Nanomaterials **11**, 114 (2021).

[18] T. Kang, Z. Ma, J. Qin, Z. Peng, W. Yang, T. Huang, S. Xian, S. Xia, W. Yan, Y. Yang, Z. Sheng, J. Shen, C. Li, L. Deng, and L. Bi, Large-scale, power-efficient Au/VO_2 active metasurfaces for ultrafast optical modulation, Nanophotonics **10**, 909 (2020).

[19] C. Chen, X. Yi, X. Zhao, and B. Xiong, Characterizations of VO_2-based uncooled microbolometer linear array, Sens. Actuators A **90**, 212 (2001).

[20] I. A. Mogunov, S. Lysenko, A. E. Fedianin, F. E. Fernández, A. Rúa, A. J. Kent, A. V. Akimov, and A. M. Kalashnikova, Large non-thermal contribution to picosecond strain pulse generation using the photo-induced phase transition in VO_2, Nat. Commun. **11**, 1690 (2020).

[21] P. Baum, D. S. Yang, and A. H. Zewail, 4D visualization of transitional structures in phase transformations by electron diffraction, Science **318**, 788 (2007).

[22] V. R. Morrison, R. P. Chatelain, K. L. Tiwari, A. Hendaoui, A. Bruhács, M. Chaker, and B. J. Siwick, A photoinduced metal-like phase of monoclinic VO_2 revealed by ultrafast electron diffraction, Science **346**, 445 (2014).

[23] S. Wall, S. Yang, L. Vidas, M. Chollet, J. M. Glownia, M. Kozina, T. Katayama, T. Henighan, M. Jiang, T. A. Miller, D. A. Reis, L. A. Boatner, O. Delaire, and M. Trigo, Ultrafast disordering of vanadium dimers in photoexcited VO_2, Science **362**, 572 (2018).

[24] L. Vidas, D. Schick, E. Martinez, D. Perez-Salinas, A. Ramos-Álvarez, S. Cichy, S. Batlle-Porro, A. S. Johnson, K. A. Hallman, R. F. Haglund, and S. Wall, Does VO_2 host a transient monoclinic metallic phase? Phys. Rev. X **10**, 031047 (2020).

[25] K. Okazaki, S. Sugai, Y. Muraoka, and Z. Hiroi, Role of electron-electron and electron-phonon interaction effects in the optical conductivity of VO_2, Phys. Rev. B **73**, 165116 (2006).

[26] A. S. Belozerov, M. A. Korotin, V. I. Anisimov, and A. I. Poteryaev, Monoclinic M1 phase of VO_2: Mott-Hubbard versus band insulator, Phys. Rev. B **85**, 045109 (2012).

[27] F. Grandi, A. Amaricci, and M. Fabrizio, Unraveling the Mott-Peierls intrigue in vanadium dioxide, Phys. Rev. Res. **2**, 013298 (2020).

[28] O. Nájera, M. Civelli, V. Dobrosavljevic, and M. J. Rozenberg, Resolving the VO_2 controversy: Mott mechanism dominates the insulator-to-metal transition, Phys. Rev. B **95**, 035113 (2017).

[29] S. Zhang, J. Y. Chou, and L. J. Lauhon, Direct correlation of structural domain formation with the metal insulator transition in a VO_2 nanobeam, Nano Lett. **9**, 4527 (2009).

[30] X. Wu, Y. Tao, L. Dong, Z. Wang, and Z. Hu, Preparation of VO_2 nanowires and their electric characterization, Mater. Res. Bull. **40**, 315 (2005).

[31] S. S. Majid, A. Ahad, F. Rahman, V. Sathe, and D. Shukla, Unveiling the role of VO_2 (b) polymorph in the insulator-metal transition of VO_2 (m1) thin films, Phys. Status Solidi B **259**, 2200108 (2022).

[32] J.-C. Orlianges, J. Leroy, A. Crunteanu, R. Mayet, P. Carles, and C. Champeaux, Electrical and optical properties of vanadium dioxide containing gold nanoparticles deposited by pulsed laser deposition, Appl. Phys. Lett. **101**, 133102 (2012).

[33] Z. Yang, C. Ko, and S. Ramanathan, Metal-insulator transition characteristics of VO_2 thin films grown on Ge(100) single crystals, J. Appl. Phys. **108**, 073708 (2010).

[34] C. N. Berglund and H. J. Guggenheim, Electronic properties of VO_2 near the semiconductor-metal transition, Phys. Rev. **185**, 1022 (1969).

[35] J. Wei, Z. Wang, W. Chen, and D. H. Cobden, New aspects of the metal-insulator transition in single-domain vanadium dioxide nanobeams, Nat. Nanotechnol. **4**, 420 (2009).

[36] J. Cao, W. Fan, K. Chen, N. Tamura, M. Kunz, V. Eyert, and J. Wu, Constant threshold resistivity in the metal-insulator transition of VO_2, Phys. Rev. B **82**, 241101(R) (2010).

[37] A. Sohn, T. Kanki, K. Sakai, H. Tanaka, and D.-W. Kim, Fractal nature of metallic and insulating domain configurations in a VO_2 thin film revealed by Kelvin probe force microscopy, Sci. Rep. **5**, 10417 (2015).

[38] M. M. Qazilbash, M. Brehm, B.-G. Chae, P.-C. Ho, G. O. Andreev, B.-J. Kim, S. J. Yun, A. V. Balatsky, M. B. Maple, F. Keilmann, H.-T. Kim, and D. N. Basov, Mott transition in VO_2 revealed by infrared spectroscopy and nano-imaging, Science **318**, 1750 (2007).

[39] A. S. Johnson, D. Perez-Salinas, K. M. Siddiqui, S. Kim, S. Choi, K. Volckaert, P. E. Majchrzak, S. Ulstrup, N. Agarwal, K. Hallman, R. F. Haglund, C. M. Günther, B. Pfau, S. Eisebitt, D. Backes, F. Maccherozzi, A. Fitzpatrick, S. S. Dhesi, P. Gargiani, M. Valvidares *et al.*, Ultrafast X-ray imaging of the light-induced phase transition in VO_2, Nat. Phys. **19**, 215 (2023).

[40] B. T. O'Callahan, A. C. Jones, J. H. Park, D. H. Cobden, J. M. Atkin, and M. B. Raschke, Inhomogeneity of the ultrafast insulator-to-metal transition dynamics of VO_2, Nat. Commun. **6**, 6849 (2015).

[41] H. von Helmholtz, Die Thermodynamik chemischer Vorgänge, Sitzungsberichte der königlich preussischen Akademie der Wissenschaften zu Berlin **1**, 22 (1882).

[42] B.-G. Chae, H.-T. Kim, S.-J. Yun, B.-J. Kim, Y.-W. Lee, D.-H. Youn, and K.-Y. Kang, Highly oriented VO_2 thin films prepared by sol-gel deposition, Electrochem. Solid State Lett. **9**, C12 (2006).

[43] M. Rodriguez-Vega, M. T. Simons, E. Radue, S. Kittiwatanakul, J. Lu, S. A. Wolf, R. A. Lukaszew, I. Novikova, and E. Rossi, Effect of inhomogeneities and substrate on the dynamics of the metal-insulator transition in VO_2 thin films, Phys. Rev. B **92**, 115420 (2015).

[44] A. Pergament, Metal-insulator transition: The Mott criterion and coherence length, J. Phys.: Condens. Matter **15**, 3217 (2003).

[45] N. Metropolis, A. W. Rosenbluth, M. N. Rosenbluth, A. H. Teller, and E. Teller, Equation of state calculations by fast computing machines, J. Chem. Phys. **21**, 1087 (1953).

[46] M. M. Qazilbash, A. Tripathi, A. A. Schafgans, B.-J. Kim, H.-T. Kim, Z. Cai, M. V. Holt, J. M. Maser, F. Keilmann, O. G. Shpyrko, and D. N. Basov, Nanoscale imaging of the electronic and structural transitions in vanadium dioxide, Phys. Rev. B **83**, 165108 (2011).

[47] W. Melitz, J. Shen, A. C. Kummel, and S. Lee, Kelvin probe force microscopy and its application, Surf. Sci. Rep. **66**, 1 (2011).

[48] M. Rosenblatt, Remarks on some nonparametric estimates of a density function, Ann. Math. Stat. **27**, 832 (1956).

[49] E. Parzen, On estimation of a probability density function and mode, Ann. Math. Stat. **33**, 1065 (1962).

[50] J. Theiler, Estimating fractal dimension, J. Opt. Soc. Am. A **7**, 1055 (1990).

[51] Chen, The solutions to the uncertainty problem of urban fractal dimension calculation, Entropy **21**, 453 (2019).

[52] F. Hausdorff, Dimension und äusseres Mass, Math. Ann. **79**, 157 (1919).

[53] B. J. Florio, P. D. Fawell, and M. Small, The use of the perimeter-area method to calculate the fractal dimension of aggregates, Powder Technol. **343**, 551 (2019).

[54] B. B. Mandelbrot, *The Fractal Geometry of Nature* (Freeman, New York, 1983).

[55] B. Klinkenberg, A review of methods used to determine the fractal dimension of linear features, Math. Geol. **26**, 23 (1994).

[56] D. Fu, K. Liu, T. Tao, K. Lo, C. Cheng, B. Liu, R. Zhang, H. A. Bechtel, and J. Wu, Comprehensive study of the metal-insulator transition in pulsed laser deposited epitaxial VO_2 thin films, J. Appl. Phys. **113**, 043707 (2013).

[57] See Supplemental Material at http://link.aps.org/supplemental/10.1103/PhysRevResearch.5.043272 for movie.

[58] T. C. Koethe, Z. Hu, M. W. Haverkort, C. Schüßler-Langeheine, F. Venturini, N. B. Brookes, O. Tjernberg, W. Reichelt, H. H. Hsieh, H.-J. Lin, C. T. Chen, and L. H. Tjeng, Transfer of spectral weight and symmetry across the metal-insulator transition in VO_2, Phys. Rev. Lett. **97**, 116402 (2006).

[59] S. Lee, T. L. Meyer, C. Sohn, D. Lee, J. Nichols, D. Lee, S. S. A. Seo, J. W. Freeland, T. W. Noh, and H. N. Lee, Electronic structure and insulating gap in epitaxial VO_2 polymorphs, APL Mater. **3**, 126109 (2015).

[60] V. Théry, A. Boulle, A. Crunteanu, J. C. Orlianges, A. Beaumont, R. Mayet, A. Mennai, F. Cosset, A. Bessaudou, and M. Fabert, Role of thermal strain in the metal-insulator and structural phase transition of epitaxial VO_2 films, Phys. Rev. B **93**, 184106 (2016).

[61] R. Bharathi, R. Naorem, and A. M. Umarji, Metal-insulator transition characteristics of vanadium dioxide thin films synthesized by ultrasonic nebulized spray pyrolysis of an aqueous combustion mixture, J. Phys. D: Appl. Phys. **48**, 305103 (2015).

[62] Z. Yang, S. Hart, C. Ko, A. Yacoby, and S. Ramanathan, Studies on electric triggering of the metal-insulator transition in VO_2

thin films between 77 K and 300 K, J. Appl. Phys. **110**, 033725 (2011).

[63] D. Maurer, A. Leue, R. Heichele, and V. Müller, Elastic behavior near the metal-insulator transition of VO_2, Phys. Rev. B **60**, 13249 (1999).

[64] J. H. Park, J. M. Coy, T. S. Kasirga, C. Huang, Z. Fei, S. Hunter, and D. H. Cobden, Measurement of a solid-state triple point at the metal-insulator transition in VO_2, Nature (London) **500**, 431 (2013).

[65] M. Liu, M. Wagner, J. Zhang, A. McLeod, S. Kittiwatanakul, Z. Fei, E. Abreu, M. Goldflam, A. J. Sternbach, S. Dai, K. G. West, J. Lu, S. A. Wolf, R. D. Averitt, and D. N. Basov, Symmetry breaking and geometric confinement in VO_2: Results from a three-dimensional infrared nano-imaging, Appl. Phys. Lett. **104**, 121905 (2014).

[66] R. Stuckert, A. Lüders, A. Wittemann, and P. Nielaba, Phase behaviour in 2D assemblies of dumbbell-shaped colloids generated under geometrical confinement, Soft Matter **17**, 6519 (2021).

[67] N. Sprinkart, D. Kazenwadel, R. Hartmann, and P. Baum, Liquid-diffusion-limited growth of vanadium dioxide single crystals, Phys. Rev. Res. **5**, 013028 (2023).